VIP High-Pressure Perovskites

DOI: 10.1002/anie.201208553

Perovskite-like Mn_2O_3: A Path to New Manganites**

Sergey V. Ovsyannikov, Artem M. Abakumov, Alexander A. Tsirlin, Walter Schnelle, Ricardo Egoavil, Jo Verbeeck, Gustaaf Van Tendeloo, Konstantin V. Glazyrin, Michael Hanfland, and Leonid Dubrovinsky*

Among complex oxides, perovskite-based manganites play a special role in science and technology.[1,2] They demonstrate colossal magnetoresistance,[3] and can be employed as memory and resistive switching elements[4] or multiferroics.[5] The perovskite structure ABO_3 has two different cation sites: *B*-sites that are octahedrally coordinated by oxygen, and cuboctahedrally-coordinated (often heavily distorted) *A*-sites.[6] The magnetic and transport properties of perovskite manganites are largely determined by the Mn–O–Mn interactions in the perovskite framework of corner-sharing MnO_6 octahedra. Although the *A* cations do not directly participate in these interactions, they control the Mn valence and the geometry of the Mn–O–Mn bonds. Complex phenomena, such as charge and orbital ordering, often accompany chemical substitutions on the *A*-site.

Requirements on formal charge and ionic radius are usually different for cations adopting the *A* or *B* positions and prevent *A*/*B* mixing. Small and often highly charged transition-metal *B*-cations are unfavorable for the large 12-coordinated *A*-site. Partial filling of the *A*-position with transition metals is, nevertheless, possible in a unique class of *A*-site ordered perovskites $AA'_3B_4O_{12}$ (where A = alkali, alkali-earth, rare-earth, Pb, or Bi cations, $A' = Cu^{2+}$ or Mn^{3+}, and B = transition metals, Ga, Ge, Sb, or Sn).[2,7] A key ingredient of such compounds is the A' cation that should be prone to a first-order Jahn–Teller effect (Cu^{2+} or Mn^{3+}). An oxygen environment suitable for such transition-metal cations at the A' position is created by the $a^+a^+a^+$ octahedral tilt system (in Glazer's notation)[8] with a notably large magnitude of the tilt (for example, in $CaCu_3Ti_4O_{12}$ the Ti–O–Ti bond angle is only 140.7°).[9] The tilt creates a square-planar anion coordination, favorable for Jahn–Teller-active A' cations. The $a_p/\sqrt{3} \approx 2.15$ Å (where a_p is a parameter of the perovskite subshell) separation between the A' and B transition-metal cations allows for a strong electronic interaction through an additional A'–O–B path that does not exist in conventional ABO_3 perovskites. For example, in $LaCu_3Fe_4O_{12}$, this interaction leads to an isostructural phase transition with charge transfer between the Cu and Fe cations.[10] Other exciting properties were also reported for $AA'_3B_4O_{12}$ systems, for example, a large negative thermal expansion in $SrCu_3Fe_4O_{12}$.[11]

In $AA'_3B_4O_{12}$ perovskites, $^1/_4$ of the *A*-positions are still occupied by electronically inactive cations. Their replacement with transition-metal cations would open a route to a novel class of compounds, in which magnetic and transport properties are controlled by both *B*–O–*B* and *A*–O–*B* interactions. To synthesize this new class of perovskites, we explored the phase diagram of Mn_2O_3 at high pressures and high temperatures (HP-HT). Mn_2O_3 was selected for two reasons: first, perovskites with cation sites $^7/_8$ filled by Mn ions ($AMn_3Mn_4O_{12}$) are already known.[2] Second, Mn cations show highly flexible charge states and coordination environments, and thus, could eventually be accommodated in the *A*-position of the perovskite structure. For example, the Mn^{2+} cation is sufficiently large for the *A*-position, as demonstrated by the high-pressure $MnVO_3$ perovskite with the $a^+b^-b^-$ octahedral tilting distortion.[12,13]

The idea of stabilizing Mn_2O_3 as $Mn[MnO_3]$ in the perovskite structure by HP-HT treatment goes along with previous attempts to prepare perovskite-type binary oxides under such conditions. Earlier works reported on high-pressure-driven stabilization of perovskite structure in some binary oxides, for example, in Fe_2O_3.[14] However, careful single-crystal in situ studies showed that the high-pressure phases of binary oxides adopt a $Rh_2O_3{}^{II}$-type lattice with a single cation site.[15] No unambiguous evidence of a binary oxide adopting the perovskite structure has so far been reported. We show that Mn_2O_3 does transform into a perovskite-type structure under HP-HT conditions. The resulting compound, though, is of the *A*-site-ordered perovskite type and should be considered as $MnMn_3[Mn_4O_{12}]$, instead of the simple $Mn[MnO_3]$ formula.

We examined the behavior of Mn^{III} oxide at HP-HT conditions by treating the starting pure bixbyite-structured material in a multianvil apparatus and studying the recovered

[*] Dr. S. V. Ovsyannikov, Dr. K. V. Glazyrin, Prof. Dr. L. Dubrovinsky
Bayerisches Geoinstitut, Universität Bayreuth
Universitätsstrasse 30, 95447 Bayreuth (Germany)
E-mail: sergey.ovsyannikov@uni-bayreuth.de
Prof. A. M. Abakumov, Dr. R. Egoavil, Prof. J. Verbeeck, Prof. G. Van Tendeloo
EMAT, University of Antwerp
Groenenborgerlaan 171, 2020 Antwerp (Belgium)
Dr. A. A. Tsirlin, Dr. W. Schnelle
Max Planck Institute for Chemical Physics of Solids
Nöthnitzer Strasse 40, 01187 Dresden (Germany)
Dr. M. Hanfland
European Synchrotron Radiation Facility (ESRF)
6 Rue Jules Horowitz, BP 220, 38043 Grenoble Cedex (France)

[**] This work was supported by the DFG (project OV-110/1-1), Alexander von Humboldt foundation, European Union Council (FP7)—Grant no. 246102 IFOX, European Research Council (FP7)—ERC Starting Grant no. 278510 VORTEX and ERC Grant no. 246791—COUNTATOMS, and Hercules fund from the Flemish Government.

Supporting information for this article is available on the WWW under http://dx.doi.org/10.1002/anie.201208553.

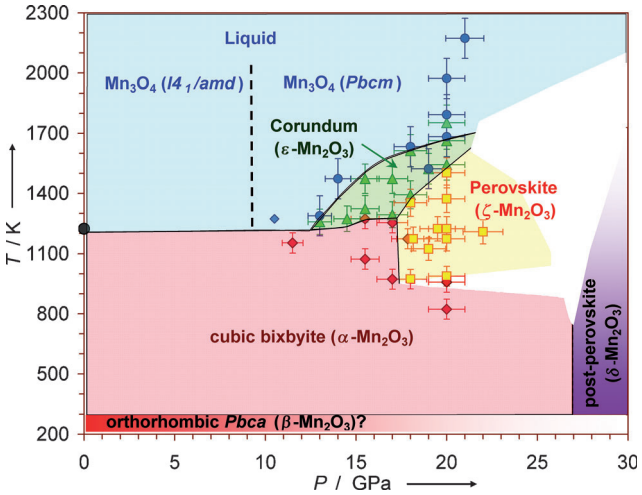

Figure 1. Pressure-temperature apparent phase diagram of Mn_2O_3 as established by HP-HT synthesis and ex situ studies. During melting (blue area) Mn_2O_3 irreversibly reduces to Mn_3O_4. A transition to the post-perovskite phase is expected above approximately 27 GPa.[20,22] The tetragonal γ-Mn_2O_3 is an alternative but rarely appearing ambient form of Mn_2O_3. The region of its stability is unknown.

samples ex situ. Heating of Mn_2O_3 at moderate temperatures (below approximately 1150–850 K, depending on pressure) and pressures between 10 to 22 GPa did not result in any transformation (Figure 1, also see Supporting Information, Table S1, Figure S1–S3). When the material was heated above 1300–1600 K in the same pressure range, it self-reduced[16] to the orthorhombic (space group *Pbcm*) high-pressure phase Mn_3O_4 (Figure 1).[17] Synthesis at intermediate temperatures allowed us to fabricate two new chemically pure phases of Mn_2O_3 (ε-Mn_2O_3 and ζ-Mn_2O_3 in Figure 1). The crystal structures of these phases were solved by using high-quality powder X-ray diffraction (XRD) data collected at the SNBL and ID31 beam-lines at ESRF under ambient conditions (see Supporting Information). The lower part of the P-T diagram (Figure 1) also deserves investigation, but it is beyond the scope of the present work.

Presently, four modifications of Mn_2O_3 are known (Table S2), namely, the cubic bixbyite α-Mn_2O_3 (space group $Ia\bar{3}$) stable at ambient conditions, the low-temperature orthorhombically distorted bixbyite-like β-Mn_2O_3 (space group *Pbca*),[18] the spinel-like γ-Mn_2O_3 with tetragonal symmetry (space group $I4_1/amd$),[19] and the $CaIrO_3$-type phase δ-Mn_2O_3 (space group *Cmcm*) synthesized above 28 GPa (unquenchable at ambient conditions).[20] Hence, we labeled the two newly synthesized phases that are metastable at ambient conditions as ε-Mn_2O_3 and ζ-Mn_2O_3. Note that some monoclinic phase of Mn_2O_3 was also reported to appear above 18 GPa,[21] but it was not seen in further studies.[20,22]

The corundum-type ε-Mn_2O_3 structure can be refined in the space group $R\bar{3}c$ (no. 167), $a = 5.0282(9)$ Å, $c = 14.1125(7)$ Å, $V = 309.01(3)$ Å^3, $Z = 6$, the atomic positions: Mn (0, 0, 0.3514(9)), O (0.3102(1), 0, 0.25)[*] (see Supporting Information, Figure S4 for the Rietveld profile). This phase is about 1 % denser than the ambient cubic bixbyite-structured α-Mn_2O_3. A detailed analysis of ε-Mn_2O_3 is beyond the scope of the present work. We only note that this phase demonstrates a similarity in the high-pressure behavior of Mn^{III} oxide and sesquioxides of Al, Fe, Cr, In, Ga, among others.[14,23]

The diffraction pattern of ζ-Mn_2O_3 (Figure 2a) is distinctly different from any known Mn oxide. The intensity distribution on the powder XRD patterns is reminiscent of a perovskite structure with a subcell of $a_p \approx 3.67$ Å. The electron diffraction patterns suggest a face-centered triclinically distorted supercell with $a = 4a_p \approx 14.7$ Å (Supporting Information, Figure S5). The perovskite-type structure of ζ-

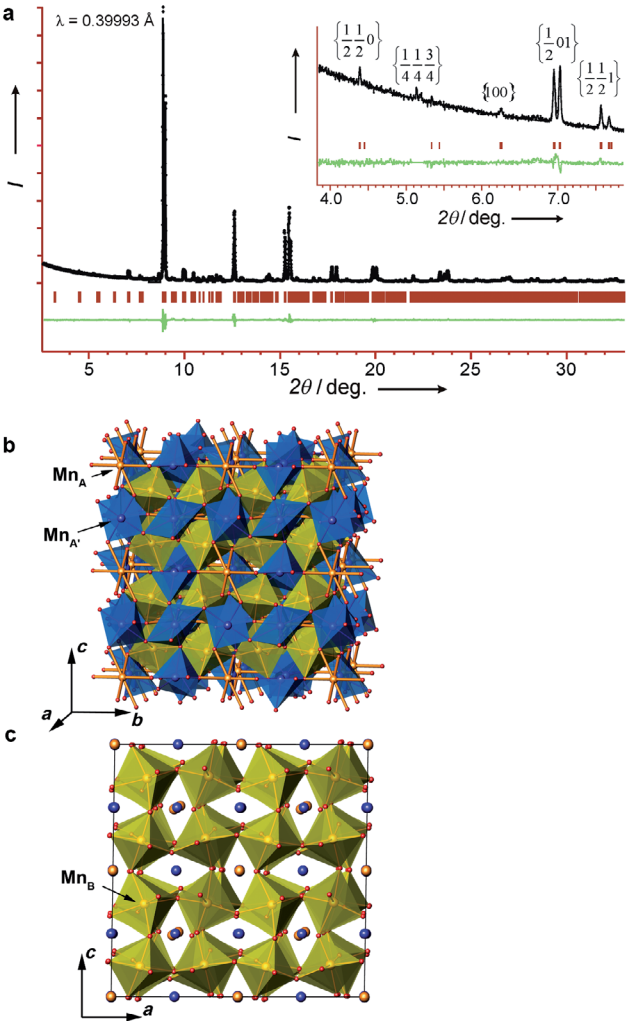

Figure 2. Crystal structure of the perovskite-type ζ-Mn_2O_3. a) Rietveld refinement profile; the inset shows the low-angle part with the superstructure reflections indexed in the a_p perovskite subcell. Vertical bars (brown) mark the reflection positions for the triclinic $4a_p \times 4a_p \times 4a_p$ unit cell used in the Rietveld refinement; the lowermost curve (green) is the difference between the experimental and calculated profiles. b) The crystal structure of ζ-Mn_2O_3. The Mn_B cations are situated in the yellow octahedra, $Mn_{A'}$ cations are at the centers of the blue tetragonal pyramids and octahedra, Mn_A cations are shown as brown spheres. Oxygen atoms are shown as small red spheres. c) The framework of corner-sharing Mn_BO_6 octahedra demonstrating the in-phase cooperative tilting distortion.

[*] Calculated density, $\rho = 5.0887(8)$ g cm^{-3}. $R_p = 0.031$ and $wR_p = 0.046$.

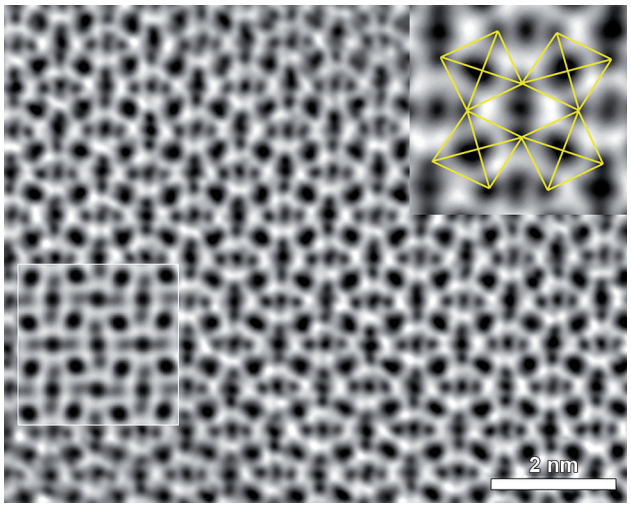

Figure 3. ABF-STEM image of ζ-Mn_2O_3 taken along the $\langle 100\rangle_p$ perovskite direction. Inset: projections of the corner-sharing in-phase tilted MnO_6 octahedra (yellow lines). The dots between the octahedra indicate the projections of the Mn atomic columns at the perovskite *A*-sites. The inserted calculated [001] ABF-STEM image (white box) was obtained with the atomic coordinates of ζ-Mn_2O_3 (Table S10) at a thickness $t = 79$ Å.

Mn_2O_3 can be directly visualized using annular bright-field scanning transmission electron microscopy (ABF-STEM; Figure 3). A perovskite octahedral framework with heavily tilted MnO_6 octahedra is clearly marked by the projections of the MnO and O columns on the ABF-STEM image (Figure 3).

The crystal structure of ζ-Mn_2O_3 was determined within the $a = 4a_p$ supercell (space group $F\bar{1}$ (no. 2, $P\bar{1}$ in the standard settings), $a = 14.6985(2)$, $b = 14.6482(2)$, $c = 14.6705(2)$ Å, $\alpha = 89.2108(8)$, $\beta = 89.2031(9)$, $\gamma = 89.196(1)°$, $V = 3157.73(9)$ Å^3, $Z = 64$;[*] see Supporting Information, Table S9, S10, S11, and Figure 2a, Figure S7 for the Rietveld profiles). This structure (Figure 2b,c) is a distorted variant of the $AA'_3B_4O_{12}$ perovskite with an $a^+b^+c^+$ octahedral tilt system. The Mn_BO_6 octahedra in ζ-Mn_2O_3 are noticeably deformed with the Mn_B–O interatomic distances in the range of 1.82–2.20 Å and subjected to a significant in-phase tilt around all three perovskite cubic axes with a magnitude of approximately 15–18° (Figure 2c).

The cooperative tilt of the Mn_BO_6 octahedra creates a distorted square-planar first coordination sphere for the $Mn_{A'}$ cations with $d(Mn_{A'}\text{-O}) = 1.81$–$2.09$ Å. The second coordination sphere of the $Mn_{A'}$ cations comprises from one to two oxygen atoms positioned at much larger distances of 2.33–2.37 Å, completing the coordination environment to a distorted tetragonal pyramid or octahedron. The rotation and distortion of the Mn_BO_6 octahedra creates a distorted octahedral environment for the Mn_A cations with the Mn_A–O distances in the range of 2.24–2.69 Å. Clearly Jahn–Teller-distorted oxygen coordination and an average bond valence sum (BVS) of 3.1 suggest that the $Mn_{A'}$ positions are preferentially occupied by the Mn^{3+} cations. Octahedral environment with a somewhat larger BVS of 3.4 for the Mn_B positions may reflect the partial Mn^{4+} substitution. The Mn_A positions are strongly underbonded with an average BVS of 1.4, pointing to a partial charge separation with the Mn^{2+} cations in the Mn_A positions and the Mn^{4+} cations in the Mn_B positions. Therefore, the valence distribution in the perovskite structure could be as follows: $Mn^{2+}(Mn^{3+})_3$-$(Mn^{3.25+})_4O_{12}$. Electron energy loss spectroscopy (EELS) combined with model-based fitting allows us to measure the valence of the Mn cations.[24] We find a clearly mixed-valence situation with 14(2) % of Mn^{2+}, 72(2) % of Mn^{3+}, and 13(4) % of Mn^{4+}. This agrees with the result found from the BVS. The average valence remains 3+ within the precision of the measurement (Supporting Information, Figure S9) as expected for stoichiometric Mn_2O_3.

The compression behavior of ζ-Mn_2O_3 was studied under pressure up to 16 GPa (Figure S10). No phase transitions were detected from the angle-dispersive powder XRD data (Figure S10). Fitting the third-order Birch–Murnaghan equation of state to the "volume versus pressure" dependence we find the bulk modulus as $B_0 = 156.5(8)$ GPa and its pressure derivative as $B_0' = 9.4(4)$ (Figure S11, S12).

Above 200 K, the magnetic susceptibility (χ) of ζ-Mn_2O_3 follows the Curie–Weiss law $\chi = C/(T-\theta)$ with an effective magnetic moment of 5.5(1) μ_B and a Curie–Weiss temperature of $\theta = -320(5)$ K (Figure S14). The negative θ value confirms the predominantly antiferromagnetic nature of ζ-Mn_2O_3, while the effective moment exceeds the spin-only value of $g[S(S+1)]^{1/2} = 4.90$ μ_B for high-spin Mn^{3+} ($S = 2$, $g = 2$). A combination of Mn^{3+}, partially reduced, and partially oxidized Mn cations with an average oxidation state of +III will show a similar effective moment.

At low temperatures, magnetic susceptibility and heat capacity measurements consistently identify two phase transitions at $T_1 = 99$ K and $T_2 = 47$ K (Figure 4). The transition at T_1 is accompanied by an inflection point in the magnetic

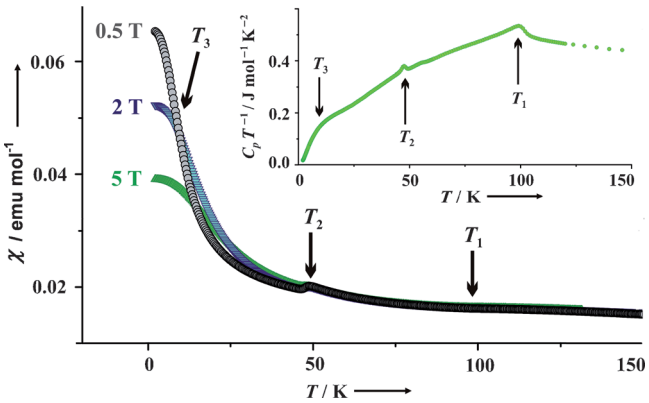

Figure 4. Magnetic susceptibility of ζ-Mn_2O_3 measured in applied fields of 0.5 T, 2 T, and 5 T. Inset: zero-field heat capacity. The characteristic temperatures of $T_1 = 99$ K, $T_2 = 47$ K, and $T_3 = 12$ K are marked with arrows.

[*] Calculated density, $\rho = 5.3115(2)$ g cm^{-3}. For synchrotron X-rays with $\lambda = 0.7021$ Å, 4–40 deg. range of 2θ and step of 0.02 deg., we found $R_F = 0.050$, $R_p = 0.022$, $R_{wp} = 0.031$. For synchrotron X-rays with $\lambda = 0.39993$ Å, 2–33 deg. range of 2θ and step of 0.004 deg., we found $R_F = 0.039$, $R_p = 0.049$, $R_{wp} = 0.070$.

susceptibility and likely indicates the antiferromagnetic ordering in ζ-Mn_2O_3. The transition at T_2 shows a weak thermal hysteresis that is characteristic for a first-order transition having a sizable structural component. However, we were unable to detect this transition in the synchrotron powder XRD data. Below $T_3 \approx 12$ K, we also observed a weak uncompensated moment of approximately 0.05 μ_B/Mn (Figure S17). Its formation is accompanied by a bend in the heat capacity (inset in Figure 4) and likely indicates a weak spin canting in the overall antiferromagnetic ground state.

Thus, Mn_2O_3 demonstrates an unprecedented example of a binary oxide that can adopt a complex distorted perovskite structure. Strong electronic coupling related to short Mn–Mn distances and efficient *A*–O–*B* interaction paths, assists in fulfilling the coordination preferences of the *A*, *A*′, and *B*-type positions. Since the *A*-type position generally requires a large cation, the respective Mn ions are partially reduced to achieve Mn^{2+} with the higher ionic radius of IR = 0.93 Å (a similar situation has been observed in the $(In_{1-x}Mn_x)MnO_3$ compounds and $MnVO_3$).[13,25] The ions in the *A*′-type positions retain the oxidation state +III (IR = 0.65 Å) to keep the strong Jahn–Teller distortion and the fourfold first coordination sphere. The *B*-type positions can accommodate Mn atoms in different oxidation states and partially host oxidized Mn^{4+} cations (IR = 0.54 Å) that balance the reduction of the Mn ions on the *A* site.

The perovskite-structured ζ-Mn_2O_3 demonstrates that new classes of perovskite materials can be fabricated by HP-HT synthesis by combining octahedral tilting distortion, Jahn–Teller deformation, and partial charge ordering. In these perovskites, the *A*-position is fully (or partially) taken up by transition-metal cations. Therefore, the role of the *A* sites is not restricted to the fine tuning of electron concentration and the *B*–O interactions. The *A* sites can be an integral part of the electronic system, thus opening broad prospects for the engineering of new materials. One could tweak the charge distribution by low-temperature oxygen/fluorine substitution and tailor the effects of colossal magnetoresistance that require a fractional oxidation state of the Mn ions. It is also possible to envisage perovskite-type compounds with an "inverted" electronic structure featuring electronically active Mn cations on the *A* site and electronically inactive cations on the *B* site. For example, a replacement of Mn^{4+} by isovalent Ti^{4+} on the *B*-sublattice of ζ-Mn_2O_3 would introduce ferroelectric displacements combined with magnetism that is driven by the remaining Mn ions on the *A* and *A*′ sites. This way, ζ-Mn_2O_3 could enable preparation of new materials relevant to multiferroics. New classes of perovskite manganites can be directly derived from Mn_2O_3 under an appropriate selection of dopants, doping level, and HP-HT conditions. Obtaining such manganites at ambient pressure can be achieved through epitaxial strain in thin films, which already demonstrated potential in stabilization of the high-pressure perovskite phases.[26]

Experimental Section

The samples were synthesized from a bixbyite-structured (a = 9.4033 Å) powder of Mn_2O_3 (Chempur, 99.99% purity) in 1200- and 5000-tonne Multi-Anvil Presses at BGI. We employed a standard assembly, which included a Re cylindrical sample capsule, $LaCrO_3$ heater, W3Re/W25Re thermocouples and an octahedral container; the procedure was similar to the one described in Ref. [27]. The samples were synthesized by heating the Mn_2O_3 powder compressed to 10–20 GPa, up to 800–2200 K. Typical synthesis times were about 2–3 h. The chemical composition of the samples was examined by scanning electron microscopy (SEM) at a LEO-1530 instrument, microprobe analysis at a JEOL JXA-8200 electron microprobe, and by ICP-MS bulk chemical analysis (Figure S2 and Table S3). The samples of ζ-Mn_2O_3 did not show any detectable non-stoichiometry.

The crystal structure of the samples was studied under ambient conditions by means of powder X-ray diffraction (XRD) at high-brilliance Rigaku diffractometer. The synchrotron XRD patterns were collected at ESRF (Grenoble, France) at the Swiss-Norwegian Beam Line, SNBL (λ = 0.7021 Å and 0.6953 Å), and at the ID31 (λ = 0.39993 Å) beam line. The compressional properties of ζ-Mn_2O_3 were studied using a diamond anvil cell with culets of 350 μm in the diameter. A sample was loaded in a hole inside a Re gasket filled with He. The study was conducted at the ID09a beam line at ESRF (λ = 0.41481 Å).

Electron diffraction (ED) patterns were obtained with a Tecnai G2 microscope operated at 200 kV. High-resolution high-angle annular dark field scanning TEM (HAADF-STEM) images and annular bright field STEM (ABF-STEM) images were obtained using a Titan G3 electron microscope operated at 300 kV and equipped with an aberration probe corrector. A monochromator is used to optimize the energy resolution for the EELS measurements to 0.17 eV while operating at an accelerating voltage of 120 kV. The measurements were performed on five different crystallites of ζ-Mn_2O_3 and the results were averaged. HAADF- and ABF-STEM image simulations were made using the QSTEM software.[28] The EELS spectra were fitted using the EELSMODEL program (http://www.eelsmodel.ua.ac.be).

Magnetic susceptibility was measured with the Quantum Design MPMS SQUID magnetometer in the temperature range 2–380 K in applied fields up to 5 T under both field-cooling (FC) and zero-field-cooling (ZFC) conditions. Heat capacity was measured with Quantum Design PPMS in the temperature range 1.8–320 K using the relaxation method.

Received: October 24, 2012
Published online: December 20, 2012

Keywords: high-pressure chemistry · magnetic properties · Mn_2O_3 · perovskite phases · solid-state structures

[1] a) J. M. D. Coey, M. Viret, S. von Molnár, *Adv. Phys.* **1999**, *48*, 167–293; b) A. Moreo, S. Yunoki, E. Dagotto, *Science* **1999**, *283*, 2034–2040; c) T. Kimura, T. Goto, H. Shintani, K. Ishizaka, T. Arima, Y. Tokura, *Nature* **2003**, *426*, 55–58; d) K. H. Ahn, T. Lookman, A. R. Bishop, *Nature* **2004**, *428*, 401–404; e) B. B. Van Aken, T. T. M. Palstra, A. Filippetti, N. A. Spaldin, *Nat. Mater.* **2004**, *3*, 164–170; f) M. Rini, R. Tobey, N. Dean, J. Itatani, Y. Tomioka, Y. Tokura, R. W. Schoenlein, A. Cavalleri, *Nature* **2007**, *449*, 72–74; g) D. Polli, M. Rini, S. Wall, R. W. Schoenlein, Y. Tomioka, Y. Tokura, G. Cerullo, A. Cavalleri, *Nat. Mater.* **2007**, *6*, 643–647; h) S. Cox, J. Singleton, R. D. McDonald, A. Migliori, P. B. Littlewood, *Nat. Mater.* **2008**, *7*, 25–30; i) F. Weber, N. Aliouane, H. Zheng, J. F. Mitchell, D. N. Argyriou, D. Reznik, *Nat. Mater.* **2009**, *8*, 798–802; j) K. Lai, M. Nakamura, W. Kundhikanjana, M. Kawasaki, Y. Tokura, M. A. Kelly, Z.-X. Shen, *Science* **2010**, *329*, 190–193; k) H. Ichikawa, S. Nozawa, T. Sato, A. Tomita, K. Ichiyanagi, M. Chollet, L. Guerin, N. Dean, A. Cavalleri, S. Adachi, T. Arima, H. Sawa, Y. Ogimoto, M.

Nakamura, R. Tamaki, K. Miyano, S. Koshihara, *Nat. Mater.* **2011**, *10*, 101 – 105.
[2] A. Prodi, E. Gilioli, A. Gauzzi, F. Licci, M. Marezio, F. Bolzoni, Q. Huang, A. Santoro, J. W. Lynn, *Nat. Mater.* **2004**, *3*, 48 – 52.
[3] a) K. Chahara, T. Ohno, M. Kasai, Y. Kozono, *Appl. Phys. Lett.* **1993**, *63*, 1990 – 1992; b) S. Jin, T. H. Tiefel, M. McCormack, R. A. Fastnacht, R. Ramesh, L. H. Chen, *Science* **1994**, *264*, 413 – 415; c) A. Urushibara, Y. Moritomo, T. Arima, A. Asamitsu, G. Kido, Y. Tokura, *Phys. Rev. B* **1995**, *51*, 14103 – 14109; d) H. Y. Hwang, S. W. Cheong, N. P. Ong, B. Batlogg, *Phys. Rev. Lett.* **1996**, *77*, 2041 – 2044; e) Y. Moritomo, A. Asamitsu, H. Kuwahara, Y. Tokura, *Nature* **1996**, *380*, 141 – 144.
[4] a) M. Filippi, W. Prellier, P. Auban-Senzier, C. R. Pasquier, *Appl. Phys. Lett.* **2008**, *93*, 142110; b) Y. Yuzhelevski, V. Markovich, V. Dikovsky, E. Rozenberg, G. Gorodetsky, G. Jung, D. A. Shulyatev, Ya. M. Mukovskii, *Phys. Rev. B* **2001**, *64*, 224428; c) D. Casa, B. Keimer, M. v. Zimmermann, J. P. Hill, H. U. Habermeier, F. S. Razavi, *Phys. Rev. B* **2001**, *64*, 100404; d) S. Balevičius, N. Žurauskienė, V. Stankevič, P. Cimmperman, S. Keršulis, A. Česnys, S. Tolvaišienė, L. L. Altgilbers, *Appl. Phys. Lett.* **2007**, *90*, 212503.
[5] a) N. A. Hill, A. Filippetti, *J. Magn. Magn. Mater.* **2002**, *242 – 245*, 976 – 979; b) T. Kimura, S. Kawamoto, I. Yamada, M. Azuma, M. Takano, Y. Tokura, *Phys. Rev. B* **2003**, *67*, 180401.
[6] R. H. Mitchell, *Perovskites*, Almaz Press Inc. **2002**, p. 318.
[7] a) G. King, P. M. Woodward, *J. Mater. Chem.* **2010**, *20*, 5785 – 5796; b) T. Locherer, R. Dinnebier, R. K. Kremer, M. Greenblatt, M. Jansen, *J. Solid State Chem.* **2012**, *190*, 277 – 284.
[8] A. M. Glazer, *Acta Crystallogr. Sect. B* **1972**, *28*, 3384 – 3392.
[9] B. Bochu, M. N. Deschizeaux, J. C. Joubert, A. Collomb, J. Chenavas, M. Marezio, *J. Solid State Chem.* **1979**, *29*, 291 – 298.
[10] Y. W. Long, N. Hayashi, T. Saito, M. Azuma, S. Muranaka, Y. Shimakawa, *Nature* **2009**, *458*, 60 – 63.
[11] I. Yamada, K. Tsuchida, K. Ohgushi, N. Hayashi, J. Kim, N. Tsuji, R. Takahashi, M. Matsushita, N. Nishiyama, T. Inoue, T. Irifune, K. Kato, M. Takata, M. Takano, *Angew. Chem.* **2011**, *123*, 6709 – 6712; *Angew. Chem. Int. Ed.* **2011**, *50*, 6579 – 6582.
[12] Y. Syono, S. Akimoto, Y. Endoh, *J. Phys. Chem. Solids* **1971**, *32*, 243 – 249.
[13] M. Markkula, A. M. Arevalo-Lopez, A. Kusmartseva, J. A. Rodgers, C. Ritter, H. Wu, J. P. Attfield, *Phys. Rev. B* **2011**, *84*, 094450.
[14] a) J. Staun Olsen, C. S. G. Cousins, L. Gerward, H. Jhans, B. J. Sheldon, *Phys. Scr.* **1991**, *43*, 327 – 330; b) S. Ono, T. Kikegawa, Y. Ohishi, *J. Phys. Chem. Solids* **2004**, *65*, 1527 – 1530.
[15] L. Dubrovinsky, T. Boffa-Ballaran, K. Glazyrin, A. Kurnosov, D. Frost, M. Merlini, M. Hanfland, V. B. Prakapenka, P. Schouwink, T. Pippinger, N. Dubrovinskaia, *High Pressure Res.* **2010**, *30*, 620 – 633.
[16] R. Metselaar, R. E. J. Van Tol, P. Piercy, *J. Solid State Chem.* **1981**, *38*, 335 – 341.
[17] C. R. Ross II, D. C. Rubie, E. Paris, *Am. Mineral.* **1990**, *75*, 1249 – 1252.
[18] S. Geller, J. A. Cape, R. W. Grant, G. P. Espinosa, *Phys. Lett. A* **1967**, *24*, 369 – 371.
[19] Z. Gui, R. Fan, X. H. Chen, Y. C. Wu, *Inorg. Chem. Commun.* **2001**, *4*, 294 – 296.
[20] J. Santillan, S.-H. Shim, G. Shen, V. B. Prakapenka, *Geophys. Res. Lett.* **2006**, *33*, L15307.
[21] T. Yamanaka, T. Nagai, T. Okada, T. Fukuda, *Z. Kristallogr.* **2005**, *220*, 938 – 945.
[22] S.-H. Shim, D. LaBounty, T. S. Duffy, *Phys. Chem. Miner.* **2011**, *38*, 685 – 691.
[23] a) A. R. Oganov, S. Ono, *Proc. Natl. Acad. Sci. USA* **2005**, *102*, 10828 – 10831; b) T. Tsuchiya, H. Yusa, J. Tsuchiya, *Phys. Rev. B* **2007**, *76*, 174108; c) A. Gurlo, D. Dzivenko, P. Kroll, R. Riedel, *Phys. Status Solidi RRL* **2008**, *2*, 269 – 271; d) S. V. Ovsyannikov, L. S. Dubrovinsky, *High Pressure Res.* **2011**, *31*, 23 – 29; e) A. Gurlo, *Angew. Chem.* **2010**, *122*, 5742 – 5744; *Angew. Chem. Int. Ed.* **2010**, *49*, 5610 – 5612.
[24] a) J. Verbeeck, S. Van Aert, *Ultramicroscopy* **2004**, *101*, 207 – 224; b) H. Tan, J. Verbeeck, A. M. Abakumov, G. VanTendeloo, *Ultramicroscopy* **2012**, *116*, 24 – 33.
[25] a) A. A. Belik, T. Furubayashi, Y. Matsushita, M. Tanaka, S. Hishita, E. Takayama-Muromachi, *Angew. Chem.* **2009**, *121*, 6233 – 6236; *Angew. Chem. Int. Ed.* **2009**, *48*, 6117 – 6120; b) A. A. Belik, Y. Matsushita, M. Tanaka, E. Takayama-Muromachi, *Angew. Chem.* **2010**, *122*, 7889 – 7893; *Angew. Chem. Int. Ed.* **2010**, *49*, 7723 – 7727.
[26] L. W. Martin, Q. Zhan, Y. Suzuki, R. Ramesh, M. Chi, N. Browning, T. Mizoguchi, J. Kreisel, *Appl. Phys. Lett.* **2007**, *90*, 062903.
[27] a) S. V. Ovsyannikov, X. Wu, V. V. Shchennikov, A. E. Karkin, N. Dubrovinskaya, G. Garbarino, L. Dubrovinsky, *J. Phys. Condens. Matter* **2010**, *22*, 375402; b) D. J. Frost, B. T. Poe, R. G. Trønnes, C. Liebske, A. Duba, D. C. Rubie, *Phys. Earth Planet. Inter.* **2004**, *143 – 144*, 507 – 514.
[28] "Determination of core structure periodicity and point defect density along dislocations": C. Koch, Ph.D. Thesis, Arizona State University, **2002**.

